High-Efficiency Dye-Sensitized Solar Cells Based on the Composite Photoanodes of SnO 2 Nanoparticles/ZnO Nanotetrapods †

ARTICLE *in* THE JOURNAL OF PHYSICAL CHEMISTRY A · DECEMBER 2009

Impact Factor: 2.69 · DOI: 10.1021/jp908747z · Source: PubMed

5 AUTHORS, INCLUDING:

Wei Chen
Huazhong University of Science and Techn…
51 PUBLICATIONS   828 CITATIONS

SEE PROFILE

Yongcai Qiu
Stanford University
73 PUBLICATIONS   2,614 CITATIONS

SEE PROFILE

Yongchun Zhong
Jinan University (Guangzhou, China)
37 PUBLICATIONS   1,108 CITATIONS

SEE PROFILE

Shihe Yang
The Hong Kong University of Science and T…
381 PUBLICATIONS   11,332 CITATIONS

SEE PROFILE

High-Efficiency Dye-Sensitized Solar Cells Based on the Composite Photoanodes of SnO₂ Nanoparticles/ZnO Nanotetrapods[†]

Wei Chen,[‡] Yongcai Qiu,[‡] Yongchun Zhong,[§] Kam Sing Wong,[§] and Shihe Yang*,[‡]

Departments of Chemistry and Physics, The Hong Kong University of Science and Technology, Clear Water Bay, Kowloon, Hong Kong, China

Received: September 10, 2009; Revised Manuscript Received: November 9, 2009

We have devised dye-sensitized solar cells (DSSCs) with >6% efficiency by employing composite photoanodes of SnO₂ nanoparticles/ZnO nanotetrapods. Benefiting from material advantages of both constituents, the composite photoanodes exhibit extremely large roughness factors, good charge collection, and tunable light scattering properties. Among the three composite photoanodes with widely differing compositions tested, the best performance (efficiency = 6.31%) was obtained with a weight ratio of SnO₂/ZnO 2:1 mainly due to the highest saturated J_{sc} achieved at a thinnest film thickness. Charge collection losses in composite films with more ZnO nanotetrapods content and thus necessarily larger film thicknesses appear to be a main limiting factor on IPCE and therefore J_{sc}, which undermines the gain from their favorable light scattering ability. An ultrathin layer of ZnO spontaneously shelled on SnO₂ nanoparticles is found to enhance V_{oc} primarily by lifting the band edges rather than by suppressing recombination. Finally, by intensity modulated photocurrent/photovoltage spectroscopy (IMPS/IMVS), we have identified that recombination in SnO₂/ZnO composite films is mainly determined by the ZnO shell condition on SnO₂, whereas electron transport is greatly influenced by the morphologies and sizes of the ZnO crystalline additives. In particular, ZnO nanotetrapods have proved to be superior in electron transport and therefore charge collection over ZnO particles additives in the SnO₂/ZnO composite-based DSSCs.

1. Introduction

Dye-sensitized solar cell (DSSC), which accomplishes efficient solar-to-electric power conversion by virtue of nanostructures,[1–3] is regarded to be a potentially low cost alternative to traditional silicon-based photovoltaics. A certified DSSC efficiency record has been pushed to >11% with a maximum IPCE up to ~85%[4,5] because of the introduction of a highly porous TiO₂ nanoparticles photoanode by O'Regan and Gratzel in 1991.[1] Many other semiconductors besides TiO₂ have also been tested as photoanode materials, and some of them, for example, SnO₂−ZnO composite (15 nm SnO₂ nanoparticles/1 μm ZnO particles 1:1 by weight),[6–8] SnO₂−MgO core−shell nanoparticles,[9] Zn₂SnO₄,[10] and so on, have achieved promising performance.[6–13] In parallel to the exploration of new photoanode materials, novel 1D nanostructures,[11,14–18] including ZnO nanowires[19,20]/nanorods[21,22] and TiO₂ nanorods[23,24]/nanotubes arrays,[25,26] have also attracted serious attention. Although their overall performance is still far from satisfactory as photoanodes because of various practical problems, they are generally superior in certain aspects of efficient DSSCs. Examples include facilitated electron transport in 1D materials such as perpendicularly aligned ZnO nanorods arrays[21,22] and TiO₂ nanotubes/nanowires arrays[25] as well as composites of nanowires/nanotubes and nanoparticles.[27,28]

Because the photoanodes of DSSCs are nanostructured by nature for effectively ferrying electrons and holes, it is of great importance to explore new materials with different architectures on the nanoscale. This cannot only enhance our understanding of the inherent working principles of DSSCs but also help to improve the cell performance,[29,30] especially in emerging frontiers such as flexible DSSCs[31] and solid-state DSSCs.[32] Most recently, our group reported a DSSC efficiency of 3.2% based on a network structured photoanode assembled from building blocks of ZnO nanotetrapods.[33] Such kind of photoanode, albeit prepared without calcination, has demonstrated incredibly long effective electron diffusion lengths. This success encouraged us to blend apposite nanoparticles into the nanotetrapods to improve further the cell performance and to elucidate the working mechanism of the composite photoanodes in the hope to realize ultimately practicable and highly efficient flexible DSSCs. We had in mind that the ZnO nanotetrapods network acts as a global electron transport highway, while the nanoparticles enclosed in and attached to the network serve to increase the roughness factor and take part in the local charge transport.[27,28,30]

Our survey experiments have shown that blending ZnO, TiO₂, or SnO₂ nanoparticles with ZnO nanotetrapods generally leads to greatly different performance features of the corresponding DSSCs. It is believed that a proper combination of the electronic structures of the constituents, for example, conduction band edge positions, which for TiO₂ is close to that of ZnO but ~500 mV higher than that of SnO₂,[34] distribution of accepting states in the conduction bands, which for SnO₂ and ZnO consist of s orbital contrary to d orbital for TiO₂,[30] is critical to the performance of composite photoanodes. In practice, different surface chemistry of the constituents has to be duly considered.

In this work, SnO₂ nanoparticles were chosen on the basis of two considerations. First, good cell performance records have already been achieved for SnO₂/ZnO composite photoanodes but with very different nanostructures.[6–8] It is tempting to see whether a similar or even higher cell efficiency can be achieved by blending SnO₂ nanoparticles with ZnO nanotetrapods.

* Corresponding author. E-mail: chsyang@ust.hk.
‡ Department of Chemistry.
§ Department of Physics.

Second, the precise functions of each component in the composite film and their synergy are yet to be elucidated.[7,35] This study aims to provide guiding principles for the search of efficient photoanodes based on binary or even ternary nanomaterials systems.

Indeed, our DSSCs based on the composite photoanodes of SnO_2 nanoparticles/ZnO nanotetrapods have reaped efficiencies comparable to or higher than the preceding record of SnO_2/ZnO composite photoanodes. The maximum photocurrent densities that can be extracted from the composite photoanodes vary only slightly when the ratio of SnO_2 nanoparticles to ZnO nanotetrapods is changed in a wide range, manifesting the outstanding charge transport property of the composite photoanodes. The structural forms and the functional roles of the ZnO component in the composite films have been carefully studied by the IMVS and IMPS methods, lending direct evidence of the origins of the V_{oc} enhancement and the J_{sc} variation of the DSSCs arising from the nanoscale blending. Moreover, ZnO nanotetrapods have proved to be excellent in electron transport (charge collection) in the composite photoanodes in comparison to particle forms of ZnO additives.

2. Experimental Section

2.1. Synthesis of SnO_2 Nanoparticles and ZnO Nanotetrapods. SnO_2 ultrafine nanoparticles were synthesized via a modified hydrothermal method from literature.[10] In a typical synthesis, 6 g $SnCl_4$·$5H_2O$ was dissolved in 80 mL of deionized water at 353 K. To this hot solution, diethylenetriamine was added dropwise under vigorous stirring until its pH reached 9.2. After the stirring was maintained at this temperature for 2 h, the initially formed white precipitates were completely dissolved, and a nearly transparent, light-yellow sol was obtained. The sol was transferred to a 100 mL Teflon-lined stainless steel autoclave, which was then heated to 453 K and kept at this temperature for 48 h. A dark-yellow gel was formed with a thin liquid layer on the top. The SnO_2 product was separated by repeated centrifugation and washing with excessive ethanol, stored in residual ethanol with the solid content of 40 wt % for later use. Details of the controlled synthesis of ZnO nanotetrapods by the metal vapor transport−oxidation method can be found elsewhere.[33,36]

2.2. Fabrication of Composite Films. For the preparation of pastes with three different SnO_2/ZnO weight ratios of 2:1, 1:1, and 1:2, 1, 0.5, and 0.25 g SnO_2 wet products (solid content = 40 wt %) were, respectively, mixed with 0.2 g ZnO nanotetrapods powder. To each mixture was added 6 mL of an ethanol/H_2O (5:1, volume ratio) solvent mixture to obtain a sol. After ultrasonic treatment of the sols for 10 min, 0.015 g PEO 2 000 000 and 0.1 g block copolymer Pluronic P123 were added with thorough stirring, forming homogeneous viscous pastes. Pure SnO_2 paste was prepared in the same way. Doctor blade technique was employed to spread the as-prepared pastes onto conductive glass substrates (FTO-coated glass, 14 Ω/square, Nippon sheet glass, Japan). The films were calcined at 450 °C in air for 30 min and then treated in 0.03 M ammonia for 30 min. After being soaked in excessive deionized water and ethanol, they were finally calcined at 450 °C for 30 min for a second time. The ammonia treatment is critical to the formation of a homogeneous ultrathin ZnO shell on SnO_2 nanoparticles (Supporting Information, Figure S1), which, as will be revealed below, plays an important role in determining the charge transport/recombination kinetics in composite photoanode-based DSSCs. For the sake of comparative studies, some films were treated with a solution of acetic acid/H_2O/ethanol 1:33:66 by

volume for 5 or 30 min, which are hereafter referred to as HAc5 and HAc30, respectively.

2.3. General Materials Characterization. Morphologies of the nanomaterials were directly examined by SEM using a JEOL 6700F at an accelerating voltage of 5 kV. TEM observations were carried out on a JEOL 2010F microscope operating at 200 kV. BET surface areas and pore size distributions of the film samples were characterized using a Coulter SA 3100 surface area analyzer. The samples for BET characterization were obtained by scratching the as-prepared films off the conductive glass substrates. XPS measurements of the film samples on glass slides were performed with Physical Electronics surface analysis equipment (model PHI 5600). XRD of the film samples on glass slides was characterized using a Philips high resolution X-ray diffraction system (model PW1825). Diffused reflectance spectra were carried out on the same film samples using a Perkin-Elmer UV/vis spectrophotometer (model Lambda 20). The film thickness was determined by a Tencor Alpha-Step 200 surface profiler system.

2.4. Solar Cell Assembly and Photoelectrochemical Characterization. The calcined films were immersed in a mixed acetonitrile/*tert*-butyl alcohol solution (1:1 in volume) containing $5 × 10^{-4}$ M N719 dye (*cis*-bis(isothiocyanato)bis(2,2′-bipyridyl-4,4′-dicarboxylato)-ruthenium(II) bis-tetrabutylammonium, Suzhou Chemsolarism, China) for 4 h. These dye-coated electrodes were assembled to make solar cells with Pt-sputtered FTO counter electrodes and acetonitrile/valeronitrile (85:15, volume ratio) electrolyte containing 0.6 M 1,2-dimethyl-3-propylimidazolium iodide, 0.03 M I_2, 0.1 M GuSCN, and 0.5 M 4-*tert*-butylpyridine. We determined the adsorbed dye amount by immersing the films in 1 mM NaOH solution (water/ethanol, 1:1, volume ratio) and monitoring the desorbed dye concentration by UV−vis spectroscopy. $J−V$ characteristic curves were recorded using a CHI 600A electrochemical analyzer. The light source (Oriel solar simulator, 450 W Xe lamp, AM 1.5 global filter) was calibrated to 1 sun (100 mW cm^{-2}) using an optical power meter (Newport, model 1916-C) equipped with a Newport 818P thermopile detector. The photoanode film area for the DSSC performance test was typically 0.25 cm^2. IPCE was measured on the basis of a Jobin-Yvon Triax 190 monochromator. Intensity-modulated photocurrent/photovoltage spectra (IMPS/IMVS) were taken by the Zahner Zennium C-IMPS system based on an IM6x electrochemical workstation, using green light-emitting diode (525 nm, LED) as the light source.

3. Results and Discussion

3.1. Nanostructural Characterizations. Shown in Figure 1A,B are TEM images of the as-synthesized SnO_2 nanoparticles. The nanoparticles are well dispersed without serious aggregation (Figure 1A), a feature that is important for film fabrication. High-resolution image and the corresponding selective area diffraction pattern (Figure 1B) show that the nanoparticles are well-crystallized with sizes in the range of 6−10 nm, much smaller than the commercial SnO_2 nanoparticles (15 nm in size) normally used in the literatures.[6,8] A typical SEM image in Figure 1C reveals a good uniformity and the unique symmetrical branching morphology (40 nm in arm diameter and 500 nm in length) of the ZnO nanotetrapods. Importantly, the branching trait of the ZnO nanotetrapots make them apt to forming 3D interpenetrating networks imbedded with small SnO_2 nanoparticles. The ZnO nanotetrapods feature four arms growing symmetrically from a common center along the ⟨0001⟩ direction (Figure 1D,E); such 1D arms not only offer a mechanically robust scaffold but also provide rapid electron transport pathways due to the minimized grain boundaries.
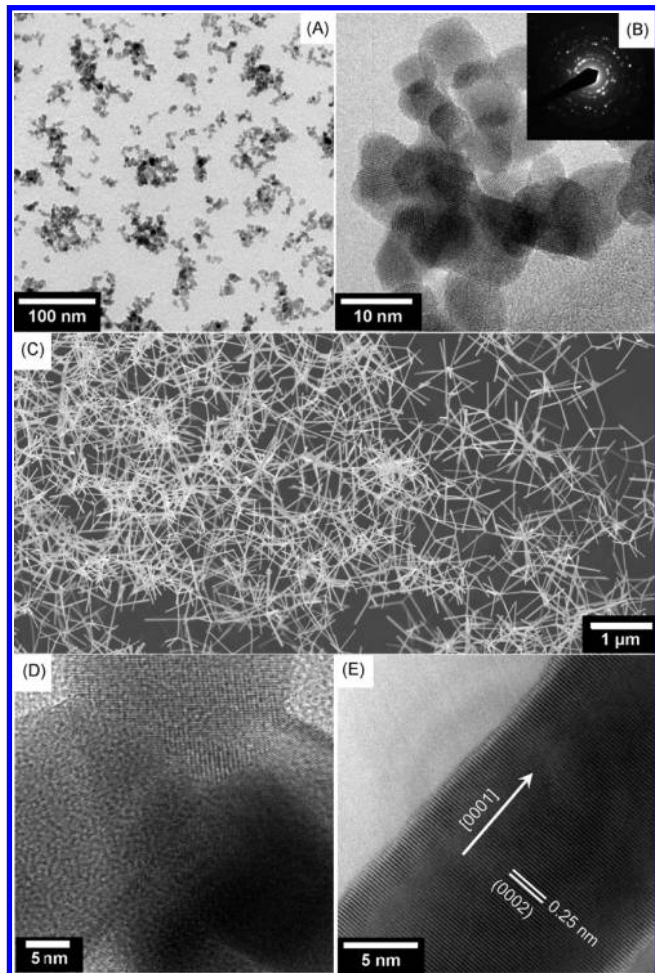
High-Efficiency Dye-Sensitized Solar Cells

J. Phys. Chem. A, Vol. 114, No. 9, 2010 **3129**

Figure 1. (A) Low-resolution and (B) high-resolution TEM images of SnO$_2$ nanoparticles. The inset in part B is the corresponding selective area electron diffraction pattern. (C) SEM image and (D,E) TEM images of ZnO nanotetrapods.

SEM images (Figure 2) reveal that pure SnO$_2$ film and SnO$_2$ nanoparticles/ZnO nanotetrapods composite films are all highly porous. In composite films, there are additional larger pores caused by the integration of ZnO nanotetrapods into the SnO$_2$ nanoparticles matrix with incompatible morphologies and length scales: some interspaces between nanotetrapods are not fully filled by nanoparticles. The more ZnO nanotetrapods are blended, the more hollow the films become, and the more optically opaque the films are because of the light scattering effect, as will be discussed below. In addition, the branched nanotetrapods are beneficial to stabilizing the composite film by releasing any locally accumulated, capillary-force-induced stress during the film drying process when freshly deposited on a FTO glass substrate. From our experience, with the higher content of ZnO nanotetrapods, thick (>10 μm), well-adhered, and crack-free composite films could be more easily fabricated (Figure 2D,F,H). For pure SnO$_2$ nanoparticles, in contrast, a crack-free film (Figure 2B) could be made to adhere to a conductive glass substrate only when it was relatively thin (<5 μm).

From XRD data (Supporting Information, Figure S2), the SnO$_2$ nanoparticles are in the tetragonal rutile phase, and the average crystal size is calculated to be 8.0 ± 0.5 nm by the Scherrer's equation, which is in accord with the TEM observations. The composite films exhibit only XRD peaks of the rutile SnO$_2$ and the wurtzite ZnO without sign of any new crystal phase such as ZnSn(OH)$_6$, ZnSnO$_3$, Zn$_2$SnO$_4$, and so on, which

is suggestive of physical blending of the two for the most part. However, when the composite film samples were interrogated by TEM-EDX (Supporting Information, Figure S3), the Zn element could always be found in the SnO$_2$ nanoparticles regions with a Zn/Sn atomic ratio of 2−5%, which indicates a situation that is more complicated than the plain blending of the SnO$_2$ nanoparticles and the ZnO nanotetrapods. No Sn was detected in the ZnO nanotetrapods regions.

To confirm the inference above, we turned to XPS. The presence of Sn−O−Zn bonds between the SnO$_2$ core and the ZnO shell is evidenced by the comparison of the Sn 3d$_{5/2}$ spectra of the composite films and the pure SnO$_2$ film. As the XPS spectra in Figure 3 show, the Sn 3d$_{5/2}$ peak is shifted to a lower energy for the composite films (486.20 eV) from that of the pure SnO$_2$ film (486.65 eV). A similar shift has been consistently observed in SnO$_2$−ZnO core−shell nanostructures compared with that of pure SnO$_2$.[35] This led us to believe that an ultrathin ZnO shell must have formed spontaneously on the SnO$_2$ nanoparticles in our SnO$_2$ nanoparticles/ZnO nanotetrapods composite film. The lower electrophilicity of Zn^{2+} in the shell than that of Sn^{4+} in the core should be responsible for the down shift of the Sn 3d$_{5/2}$ peak upon the formation of the ultrathin ZnO shell. The peak position at 486.20 eV is independent of the composition for the three composite films, indicating a similar ZnO shell coverage and thickness on SnO$_2$ under the same treatment conditions.

We suspect that the formation of the shell layer of ZnO on the SnO$_2$ nanoparticles stems from the chemical instability of ZnO in a polar solvent; the alkaline ZnO tends to be deposited on the relatively acidic surface of SnO$_2$.[8] The ammonia treatment is considered to promote this process for the full coverage of the SnO$_2$ surface with ZnO by the facilitated mass transport through the Zn(NH$_3$)$_4$$^{2+}$ complex in solution. Using an atomic ratio of 2−5% for Zn/Sn in the SnO$_2$ nanoparticles region (estimated from the TEM-EDX measurement) and assuming ideal spheres of 8 nm diameter for the SnO$_2$ nanoparticles, we estimate the ZnO shell to be only one to two atomic layers thick, which explains why the shells could not be imaged clearly, even with high-resolution TEM.[7]

Pore size distributions of film samples peeled off from conductive glass substrates are shown in Figure 4. In going from pure SnO$_2$ film to composite films with increasing ZnO content, the pore size distribution gradually becomes wider, which is consistent with their SEM images in Figure 2. For pure SnO$_2$ film, the pores are narrowly distributed at ∼13.9 nm, associated with long and narrow pore channels arising from nanoparticle hierarchical aggregation. This is inferred from its nitrogen adsorption−desorption isotherm (the inset in Figure 4), which is of the typical type IV with H1 hysteresis loop, very similar to that of mesoporous SnO$_2$ obtained by P123 surfactant directed self-assembly.[37] The long and narrow cylindrical channels are constructed by SnO$_2$ nanoparticles and templated by P123 micelles. The fitted BET surface area is 98.7 m^2 g^{-1}. For composite films, the pore size distribution becomes broader, but still ∼14 nm, with the increase in the ZnO nanotetrapod content because more irregular, polydisperse interspaces are formed and incompletely filled by the SnO$_2$ nanoparticles, for which the pure nanotetrapods film presents an extreme case. The broader pore size distributions are embodied by the shape of their nitrogen adsorption−desorption isotherms: (1) the inflection points of isotherms shift toward high relative pressure (P/P_0), corresponding to the capillary condensation of larger pores; (2) the adsorption−desorption hysteresis loops gradually transform from H1 type to H3 type associated with irregular pores because
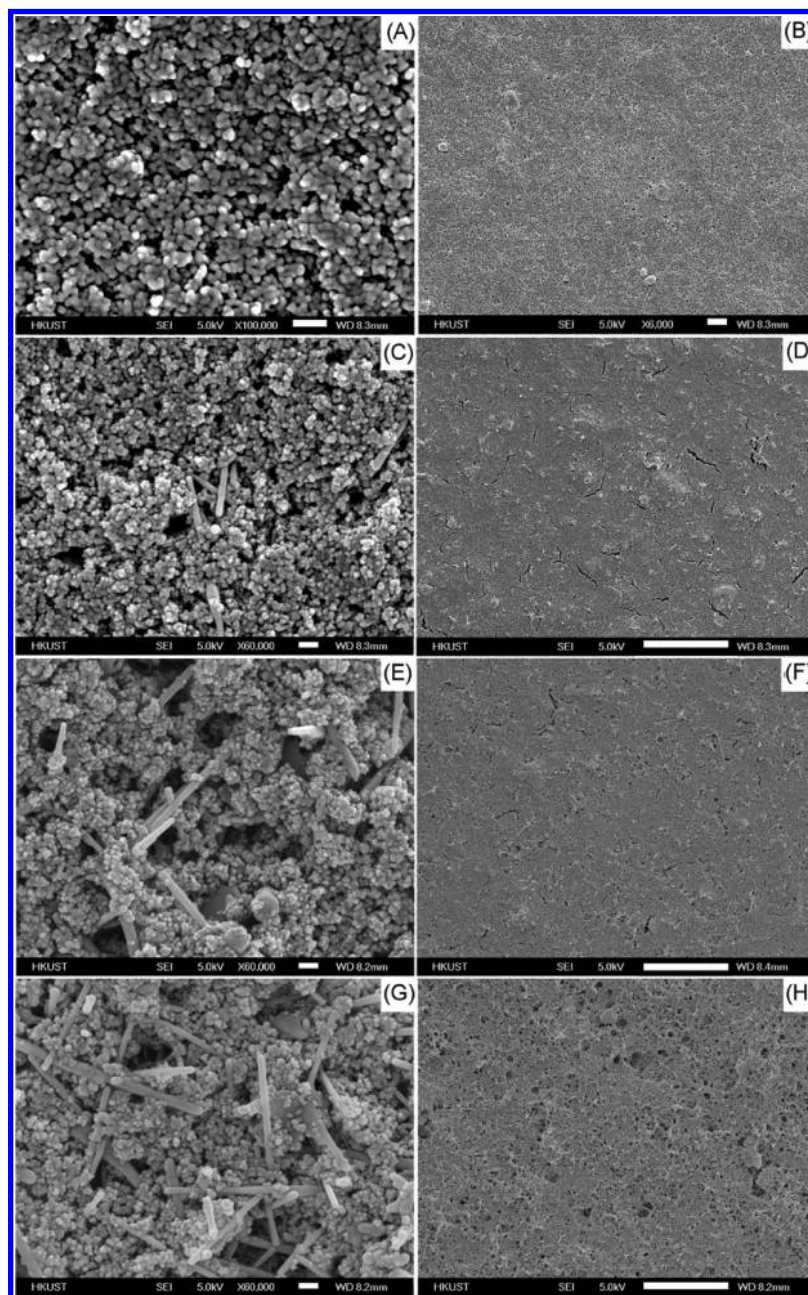
Figure 2. High-resolution and low-resolution SEM images. (A,B) Pure SnO_2 nanoparticles film. (C–H) SnO_2 nanoparticles/ZnO nanotetrapods composite films with different weight ratios: (C,D) 2:1, (E,F) 1:1, (G,H) 1:2. Scale bars: (A) 100 nm, (B) 1 μm, (C,E,G) 100 nm, (D,F,H) 10 μm.

of the loss of long and narrow cylindrical channels when more and more ZnO nanotetrapods are integrated into the SnO_2 nanoparticles matrix.

By blending SnO_2 nanoparticles with more and more ZnO nanotetrapods, BET surface areas of the composite films are gradually increased from 85.1 (SnO_2/ZnO 2:1), to 109.1 (SnO_2/ZnO 1:1), to 128.5 m^2 g^{-1} (SnO_2/ZnO 1:2). The latter two BET surface areas are even higher than that of the pure SnO_2 nanoparticles film (98.7 m^2 g^{-1}). This is unexpected because the BET surface area of the pure ZnO nanotetrapods film is relatively low (18.9 m^2 g^{-1}),[33] and blending more ZnO nanotetrapods into a composite film should have only trimmed down the BET surface area. Such abnormal phenomenon again implies that the composite films are not simply a physical blending of the ZnO nanotetrapods and the SnO_2 nanoparticles. In fact, as can be seen from Figure 4, more and more pores are distributed
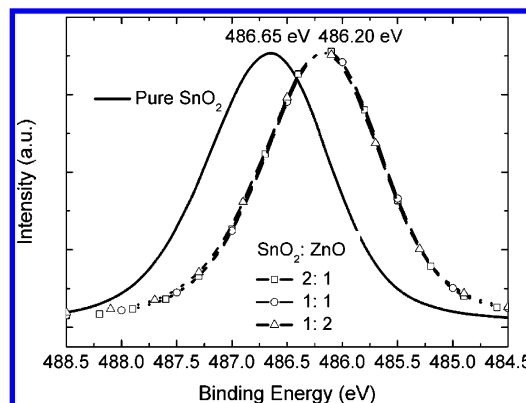

Figure 3. Sn $3d_{5/2}$ XPS spectra of pure SnO_2 nanoparticles film and the three composite films.
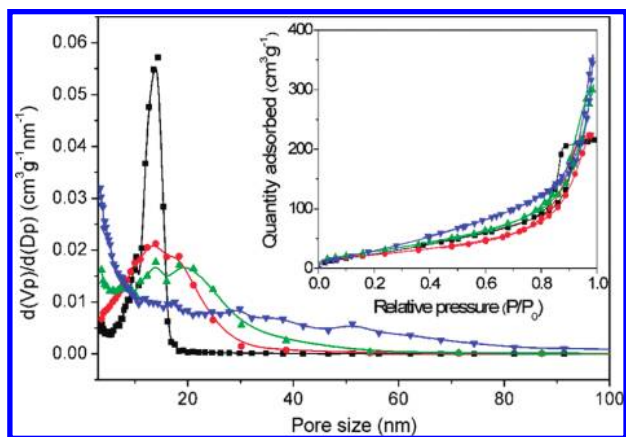
High-Efficiency Dye-Sensitized Solar Cells

J. Phys. Chem. A, Vol. 114, No. 9, 2010 **3131**

Figure 4. Pore size distributions of pure SnO_2 nanoparticles film and three SnO_2 nanoparticles/ZnO nanotetrapods composite films. The inset is the corresponding nitrogen adsorption−desorption isotherms. Black, ■: SnO_2 nanoparticles film; red, ●: SnO_2/ZnO 2:1 composite film; green, ▲: SnO_2/ZnO = 1:1 composite film; blue, ▼: SnO_2/ZnO = 1:2 composite film.
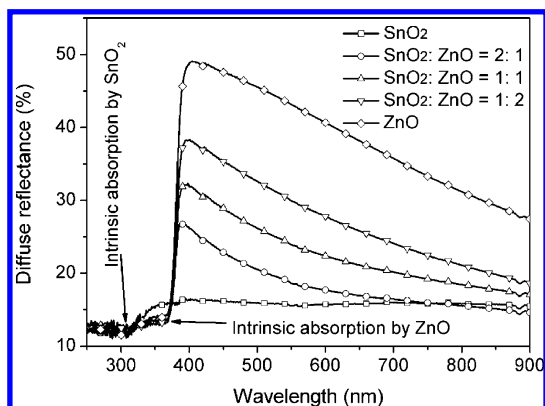

Figure 5. Diffuse reflectance spectra of pure SnO_2 nanoparticles film, pure ZnO nanotetrapods film, and three SnO_2 nanoparticles/ZnO nanotetrapods composite films. All films are prepared with the same thicknesses of ~6 μm on glass slides.

in the range of 3−6 nm as the ZnO content is increased in the composite films, which may be partially responsible for the abnormal increase in BET surface area. One of the reasons for the formation of the small pores may be hindered hierarchical aggregation of the ~8 nm SnO_2 nanoparticles as a result of the increasing incorporation of the ZnO nanotetrapods such that the pore size is mainly determined by the interspaces of the primary nanoparticle assembly. Moreover, the roughening of the ZnO and SnO_2 surfaces together with the formation of the ZnO ultrafine nanoparticles in composite films with an increasing ZnO content should also increase the BET surface area.

The difference in pore structure has a direct influence on the light scattering property of the composite films, as can be clearly perceived from their diffuse reflectance spectra in Figure 5. It should be pointed out that the dramatic reduction of reflection below 380 nm (except the pure SnO_2 film) and below 340 nm (except the pure ZnO film) is caused by the band gap transitions of ZnO (E_g = 3.2 eV) and SnO_2 (E_g = 3.6 eV), respectively. Overall, the reflectance spectra appear to abide by the Mie scattering theory, which states that pores with a comparable size to the light wavelength can act as effective light scattering centers.[38,39] Understandably, light scattering in the pure SnO_2 nanoparticles film is nearly negligible because the pores inside the film are too small (<20 nm) to act as effective scattering centers. However, the diffuse reflectance of the composite films

increases dramatically and monotonously with the increase in the ZnO content, with the utmost for the pure ZnO nanotetrapods films. Notably, a substantial fraction of visible light is scattered back. This is not surprising because more ZnO nanotetrapods blended with SnO_2 nanoparticles will generate more pores with sizes closer to ideal for light scattering, namely, 50−100 nm, as suggested by Hore et al.[38] Similar diffuse reflectance spectra arising from the scattering of voids (pores) were previously reported.[16,40]

3.2. Performance Appraisal of the Dye-Sensitized Solar Cells. Presented in Figure 6 are the performance test results of the DSSCs based on the three series of composite films under 1 Sun AM 1.5G simulated solar light. The corresponding data for the pure SnO_2 nanoparticles film and for the pure ZnO nanotetrapods film[33] are also included for comparison.

The dependence of roughness factor (RF) on film thickness for the different series of films is plotted in Figure 6A. RF was calculated by multiplying a BET surface area by the weight of a film peeled off from the glass substrate, which is then divided by the area of the film. Significantly, the RF values for the three series of composite films can exceed 1600, much higher than that of the pure ZnO nanotetrapods film and also comparable to those of the most efficient TiO_2 nanoparticles photoanodes.[41]

The dependence of dye-adsorbing amount on film thickness shows roughly similar increasing trends as those of RF (Figure 6A). It is noticed that the dye-adsorbing amount per RF for the pure SnO_2 film is obviously lower than those of composite films probably because of the more basic surfaces of the latter, that is, the ZnO ultrathin layer modified SnO_2 surfaces.[8] More to the point, because the dye-adsorbing time of 4 h in this work was optimized with respect to the composite films, it is probably too short for saturated dye adsorption on the pure SnO_2 nanoparticles film.

The dependence of short-circuit photocurrent density, J_{sc}, on film thickness exhibits obviously nonlinear arc-shaped trends (Figure 6B) for all except the ZnO nanotetrapods films. For the three series of composite films with SnO_2/ZnO 2:1, 1:1, and 1:2 compositions, J_{sc} become saturated at about 7, 10, and 15 μm, respectively. At the thicknesses of the saturated J_{sc}, the RF and dye-adsorbing amount are nearly the same, which are ~1600 and in the range of $(2.0-2.4) \times 10^{-7}$ mol·cm^{-2}, respectively. The nonlinear trends of J_{sc} versus RF (dye adsorbing amount) and their saturated positions should be primarily due to the Beer's Law, which is related to the light harvesting efficiency of a photoanode through the equation $LHE(\lambda) = 1 - 10^{-\varepsilon\Gamma}$,[42] where Γ is the surface coverage of dye (mol cm^{-2}) and ε is the dye's molar absorption coefficient (mol^{-1} cm^2) at wavelength λ. Using $\varepsilon = 1.41 \times 10^7$ mol^{-1} cm^2 for N719 dye at 515 nm,[43] we find that Γ with a value of 7.1×10^{-8} mol cm^{-2} is sufficient to secure LHE(515 nm) as high as 90%. Further increase in the dye-adsorbing amount to $(2.0-2.4) \times 10^{-7}$ mol cm^{-2} associated with the saturated J_{sc} will mainly promote harvesting of the near-infrared light, resulting in reduced increasing rate of overall light harvest and therefore reduced increasing rate of J_{sc} with the increase in RF. This is one of the reasons why the J_{sc} dependences on film thickness (or RF and dye adsorbing amount) exhibit nonlinear arc-shaped trends. Additionally, light scattering effect as revealed by diffuse reflectance spectra of the three composite films also needs be considered; the light scattering effect could cause deviation from the Beer's law[42] and thus may be partially responsible for different arc shapes of the J_{sc} thickness plots.

V_{oc} values (600−660 mV) of the three composite films (Figure 6C) are found to lie between those of the pure SnO_2 nanopar-
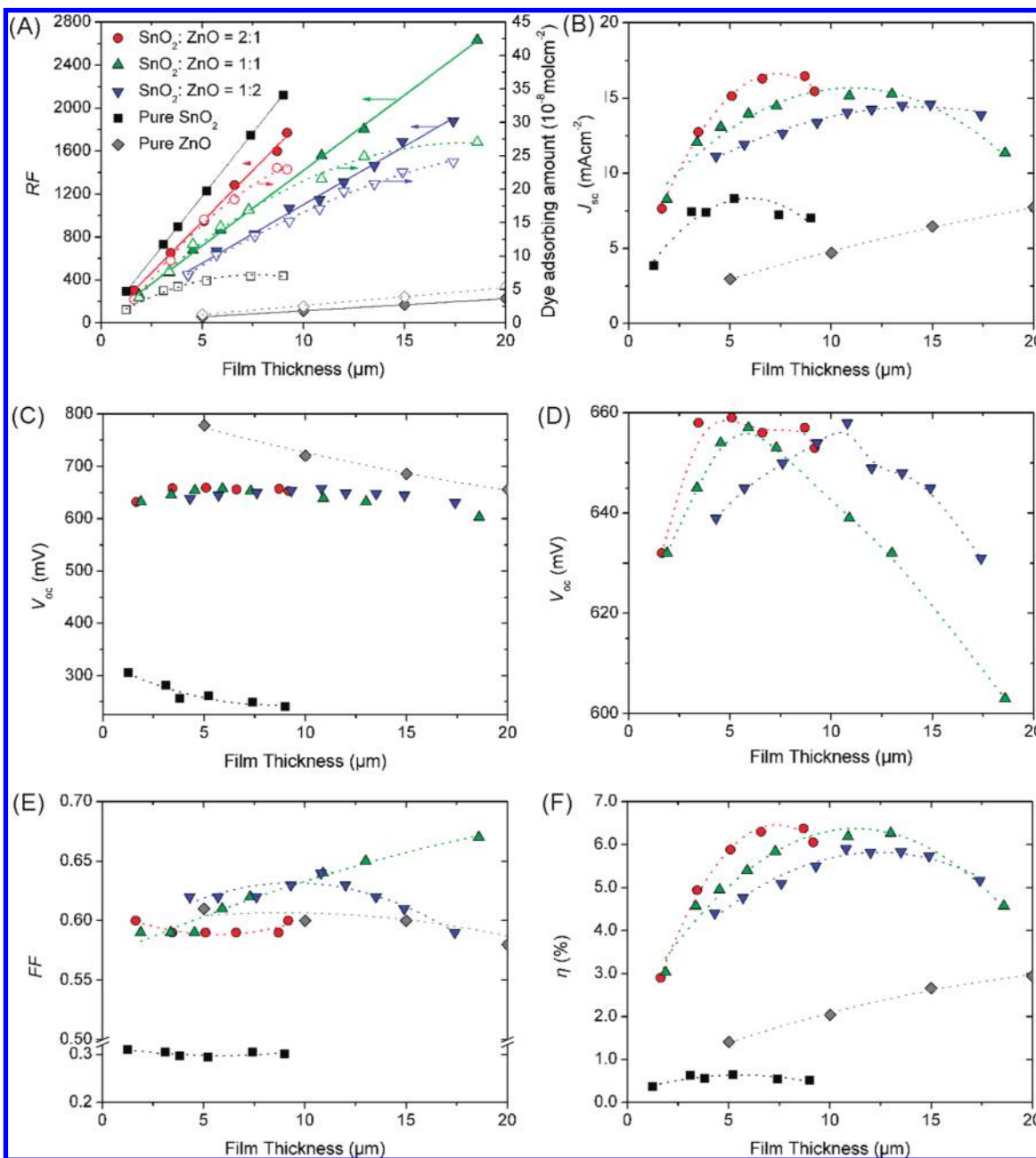
Figure 6. Thickness-dependent characteristics of the SnO_2 nanoparticles/ZnO nanotetrapods composite films as well as pure SnO_2 nanoparticles film and pure ZnO nanotetrapods film. (A) Roughness factor, RF, (■) and dye adsorbing amount (□); (B) short-circuit photocurrent density, J_{sc}; (C) open-circuit photovoltage, V_{oc}; (D) blown-up region highlights, V_{oc}, of the three composite films; (E) fill factor, FF; and (F) overall energy conversion efficiency η.

ticles film and the pure ZnO nanotetrapods film but much closer to the latter. The origin of the V_{oc} enhancement of SnO_2/ZnO composite photoanodes in comparison with pure SnO_2 has been debated since the first report on this subject.[6] We will resolve this point in latter sections of this article after presenting our new IMVS results. The V_{oc} dependences for the three composite films on thickness are similar (Figure 6D): first increase and then decrease, which seems to be at odd with the previously reported monotonically decreasing trend of V_{oc} with increasing film thickness.[10,27] The common decreasing trend of V_{oc} with film thickness is usually attributed to the increase in recombination loss, which can be qualitatively appreciated from the equation of $V_{oc} = (k_B T/q) \ln(J_{inj}/J_{dark})$,[44] where k_B, q, and T are the Boltzmann constant, electron charge, and absolute temperature, respectively, and J_{inj} is injected photocurrent density from dye to the semiconductor and J_{dark} is dark current due to the

recombination at semiconductor/electrolyte interface. The dark reaction can take place at two interfaces:[45] (1) the interface between electrolyte and bare FTO glass substrate uncovered by nanomaterials, whereat recombination is important when the active film is relatively thin; (2) the highly porous film/electrolyte interface, which may mainly be the recombination site when the roughness factor is large. Therefore, the J_{dark} can be portioned into $J_{dark,FTO}$ and $J_{dark,porousfilm}$, where the first term represents the dark current loss through FTO and the second is dark current through porous film. It is well documented that $J_{dark,FTO}$ can be abated by coating a blocking layer between FTO and active film.[46,47] Because we have not exploited an adequate blocking layer yet, the dark current loss through the bare FTO substrate may play an important role in the small thickness regime of our composite-film-based photoanodes. In this small thickness regime, as the film thickness increases, J_{inj} and

High-Efficiency Dye-Sensitized Solar Cells

J. Phys. Chem. A, Vol. 114, No. 9, 2010 **3133**

TABLE 1: Summary of the Performance Parameters of DSSCs Based on SnO₂ Nanoparticles/ZnO Nanotetrapods Composite Photoanodes

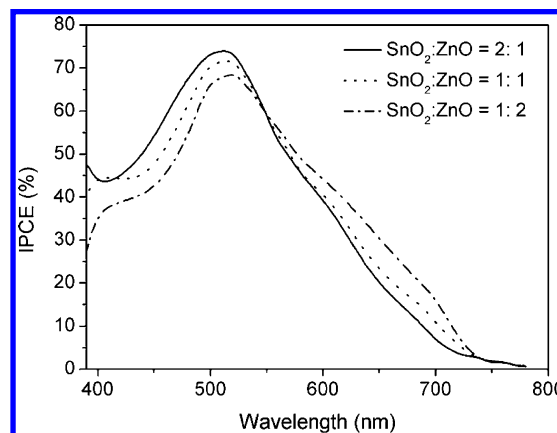| sample	thickness (μm)	V_{oc} (mV)	J_{sc} (mA cm^{-2})	FF	IPCE$_{max}$	η (%)
SnO₂/ZnO 2:1	6.6	656	16.3	0.59	74.1%	6.31
SnO₂/ZnO 1:1	10.9	639	15.1	0.64	71.5%	6.18
SnO₂/ZnO 1:2	13.5	648	14.5	0.62	67.6%	5.83

$J_{dark,porousfilm}$ both increase with thickness but more for the former, and the nearly constant $J_{dark,FTO}$ means that the ratio of J_{inj}/J_{dark} and therefore V_{oc} increase with film thickness. In the thick film regime, however, as the thickness increases, $J_{dark,porousfilm}$ becomes predominant over $J_{dark,FTO}$ and increases more rapidly than J_{inj} because of the reduced light harvest, leading to the gradual decline of the ratio of J_{inj}/J_{dark} and thus V_{oc}.

Fill factors (FFs) for the three composite films vary within the range of 0.55 to 0.7 (Figure 6E) depending on the thickness, which are generally higher than that of pure SnO₂ nanoparticles films and comparable to that of pure ZnO nanotetrapods films. Although we have not been able to account for the detailed FF dependences on film thickness at present, complications such as those arising from the peculiar nanostructures and their combinations as well as dye corrosion on ZnO in the composite films may play a part.

Maximum cell efficiencies for the three composite films obtained from Figure 6F are listed in Table 1. The efficiencies up to 6.31% are a dramatic improvement over the best SnO₂-based DSSCs (~2%)[48] and rank among the highest level for SnO₂/ZnO composite photoanode-based DSSCs.[6,8] The V_{oc} enhancement over that of the pure SnO₂ film is mainly responsible for the significant improvement in the overall efficiency of the SnO₂/ZnO composite-film-based DSSCs because pure SnO₂ photoanode itself can also yield high photocurrent.[48] On the other hand, the difference in maximum efficiency among the three composite films is within 15%, which is mainly ascribed to the difference in J_{sc}. As another noteworthy feature, our composite photoanodes achieve the best performance at the weight ratio of SnO₂/ZnO 2:1, and this contrasts with the work of Tennakone et al. on ZnO big particles/SnO₂ nanoparticles composite films, which obtained the maximum efficiency strictly at the ZnO/SnO₂ weight ratio of nearly 1:1.[6,7] Such a difference is largely a result from the peculiar structure of our nanotetrapods, which possess three-dimensionally distributed long arms and can be embedded in the SnO₂ nanoparticles matrix without occupying much space in contrast with the space-filling, micrometer-sized ZnO particles used by Tennakone et al.

3.3. Relationship between J_{sc} and IPCE. IPCEs of solar cells based on the three composite photoanodes are shown in Figure 7 and also selectively listed in Table 1. The maximum IPCE value for the three composite films at ~520 nm decreases from 74.1, to 71.5, to 67.6% with increasing content of ZnO nanotetrapods. As expected, this decreasing trend of IPCE for the composite films is naturally in keeping with the gradual drop of the maximum J_{sc} from 16.3, to 15.1, to 14.5 mA cm^{-2} with increasing ZnO content. It is also important to recognize from Figure 7 that with the increase in the ZnO content, the IPCE value in the long wavelength tail increases but suffers a comparable or higher decrease in the short wavelength region. A similar observation has also been reported on IPCE of a film in which a light scattering material was directly blended with TiO₂ nanoparticles.[43]

With respect to the IPCE variations of the three composite films, we will discuss their origins in terms of light-harvesting

Figure 7. IPCE of DSSCs based on the three typical composite photoanodes with different weight ratios, as listed in Table 1.

efficiency (LHE(λ)), electron injection yield from the dye excited state into semiconductor (Φ_{inj}), and charge collection efficiency at the front conductive glass substrate (η_{cc}).[49]

The LHE of a cell mainly depends on intrinsic properties of the dye, for example, the wavelength-dependent molar absorption coefficient and its adsorbing density on porous photoanodes, which is governed by the Beer's law.[42] For a practical solar cell such as our ZnO nanotetrapod-based DSSCs, the LHE equation should accommodate the scattering effect by introducing the concept of effective optical path length within the photoanodes. The effective optical path length can be increased by the addition of relatively large particles to small nanoparticles matrix to induce light scattering of the photoanodes, which is also called the light-trapping effect.[4,41] Such light-trapping effect leading to enhancement on IPCE especially in the near-infrared wavelength range is very important for DSSCs because the widely used Ru-pyridine-based dyes absorb light weakly in this region. In our work, the broad pore size distribution resulted in relatively strong light scattering. As reflected in Figure 5, the optical path length in the three composite films is gradually enhanced in the sequence of SnO₂/ZnO 2:1, 1:1, and 1:2. Consequently, IPCE on the red side of the spectra is gradually enhanced in this sequence, as revealed in Figure 7.

To examine the difference in electron injection yield (Φ_{inj}), we employed the time-resolved fluorescence decay method to probe the nanosecond time scale emission decays of N719 dye on the three composite films with nearly the same dye-adsorbing amount. It is well known that the fluorescence emission of N719 dye can be strongly quenched by electron injection to semiconductors with a suitable conduction band edge position such as TiO₂, SnO₂, and ZnO.[30,50] Therefore, by comparing the emission decays of the dye on the composite films, one can draw at least qualitative conclusions about the variation of injection efficiency with the film compsotion.[51,52] The emission decay profiles for the three composite films show almost the same initial intensity and a similar decreasing trend (Supporting Information, Figure S4), a biexponential decay that can be fitted by two exponential functions. The fact that the maximum difference on the integrated areas of the fitted curves is only ~10% implies that the charge injection efficiencies are nearly the same for the three composite films because Φ_{inj} is determined by the integrated area of an active film divided by that of a reference (e.g., dye on ZrO₂ or Al₂O₃ film[51,52]). The similar electron injection kinetics for the three composite films lends further evidence of the existence of an ultrathin, homogeneous ZnO shell on the SnO₂ nanoparticles, which, in combination
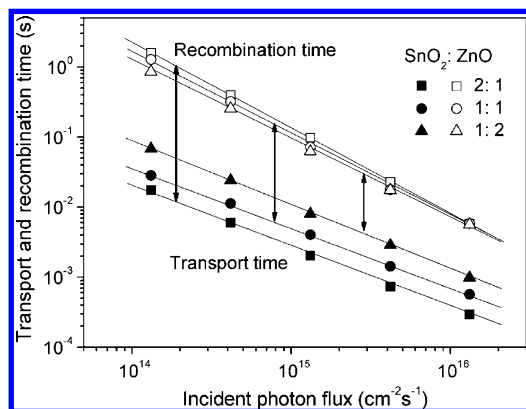
Figure 8. Incident light intensity dependent transport and recombination time constants for the SnO$_2$/ZnO nanotetrapods 2:1, 1:1, and 1:2 composite photoanodes (as listed in Table 1).

with ZnO nanotetrapods, supplies similar accepting states for electron injection.

We next consider the charge collection efficiency, η_{cc}, determined by IMPS/IMVS measurements through the following equations[25,26,53]

$$\eta_{cc} = 1 - \frac{\tau_t}{\tau_r} \qquad (1)$$

$$\tau_t = \frac{1}{\omega_t} = \frac{1}{2\pi f_t} \qquad (2)$$

$$\tau_r = \frac{1}{\omega_r} = \frac{1}{2\pi f_r} \qquad (3)$$

where τ_t and τ_r are electron transport time across the photoanode films and recombination time of electrons with I$_3^-$ ions in the electrolyte, respectively, and f_t and f_r are the characteristic frequency minimums of the IMPS and IMVS imaginary components, respectively.

Figure 8 plots τ_t and τ_r as a function of the incident photon flux (light intensity, I_0) for the three composite films. Obviously, the lower the content of ZnO nanotetrapods in a composite film, the larger the gap between τ_t and τ_r and thus the higher the change collection efficiency according to eq 1. More specifically, the charge collection efficiencies at the highest light intensity (1.32 × 10^{16} cm^{-2} s^{-1}) for the three composite films are 82.6, 90.2, and 95.0% in the order of decreasing ZnO content. Such distinct differences in the charge collection efficiency is notably parallel to the composition-dependent IPCE variations for the three composite films at 515 nm (the wavelength of the LED light source in IMPS/IMVS measurements), suggesting that η_{cc} predominates LHE and Φ_{inj} in determining IPCE for the composite films. Such a charge collection limitation naturally explains the monotonic decrease in IPCE in the short wavelength region (<515 nm) with the increase in ZnO nanotetrapod content. (See Figure 7.) On the surface, the gradual decrease in charge collection efficiency with increasing ZnO content (resulting from the increase in charge transport time but the nearly constant recombination time) seems to be contrary to our expectation that more ZnO nanotetrapods should improve charge transport. However, for the same dye-adsorbing amount and RF, photo-injected electrons need to transport a much longer distance (the film thickness) in the SnO$_2$/ZnO 1:2 composite film to reach the conductive glass substrate than in the SnO$_2$/ZnO 2:1 composite film.

From the results and discussions above, we can expect a better performance of DSSCs based on a double layer (or multilayer)

structured photoanode, of which the under layer is composed of the SnO$_2$/ZnO 2:1 composite film with a good charge collection efficiency, and the top layer consists of the SnO$_2$/ZnO 1:2 composite film with strong light scattering capability. With such a judicious combination, both high charge collection efficiency and strong light scattering can be realized in one integrated film. This experiment is currently underway in our laboratory.

3.4. Electron Transport and Recombination in the Composite Films. In the above, we have established that ZnO in the composite films exists in two forms: one is ZnO nanotetrapods and the other is ultrathin ZnO shells on SnO$_2$ nanoparticles. To clarify the roles of the ZnO nanotetrapods and the ZnO shells in charge transport and recombination kinetics in the composite films, we examined the effect of ZnO dissolution in acidic solutions on the charge transport and collection in the composite films. For this study, the SnO$_2$/ZnO 2:1 and 1:1 composite films were chosen and treated with 1% HAc in EtOH/ H$_2$O (1:2 by volume) for 5 or 30 min (denoted as samples HAc5 and HAc30, respectively) to dissolve ZnO partially or totally, resulting in SnO$_2$ nanoparticles/ZnO particles composite film (HAc5) or nearly pure SnO$_2$ nanoparticles films (HAc30). The structural differences between HAc5 and HAc30 have been confirmed by XRD and TEM. (See Figure S5 in Supporting Information.) Corrosion of ZnO nanotetrapods yields new pore channels, leading to deteriorated continuity in the nanoparticles network. Figure 9 compares typical images of the SnO$_2$/ZnO 1:1 composite film before and after HAc treatment, highlighting the corrosion induced porosity and the resulting discontinuity of the electron transport network. Such a scenario is definitely maintained in the SnO$_2$/ZnO 2:1 composite film, albeit to a lesser extent because of the lower ZnO nanotetrapods content. The differences between HAc-treated films and their original films not only lie in the changed nanotetrapods' shape (HAc5 contains residual ZnO particles derived from partially dissolved nanotetrapods, whereas no ZnO crystalline particles can be found in HAc30) but also relate to the altered ZnO shell thickness on SnO$_2$ nanoparticles. The gradual trimming down of the ZnO shell on SnO$_2$ with increasing HAc treatment time was revealed by XPS spectra in the core level region of Sn 3d$_{5/2}$ of the HAc5 and HAc30 films (SnO$_2$/ZnO 2:1) (Figure S6, Supporting Information). The gradual upshift of the Sn 3d$_{5/2}$ peak demonstrates the steady decrease in the ZnO shell thickness, which is consistent with the XPS result of Niinobe et al.[35]

Effects of acid treatment of composite films on $J-V$ characteristic curves are shown in Figure 10. In general, V_{oc} is dramatically decreased with the gradual loss of ZnO content upon HAc treatment. Interestingly, although J_{sc} for the SnO$_2$/ ZnO 2:1 composite film is nearly unchanged with the loss of ZnO, J_{sc} for the SnO$_2$/ZnO 1:1 composite film experiences a considerable decrease. To understand the $J-V$ characteristic curves, we studied the electron transport and recombination kinetics by using the IMPS/IMVS methods.

Plotted in Figure 11 are τ_t and τ_r versus the incident photon flux for the composite films of SnO$_2$/ZnO 2:1 (A) and SnO$_2$/ ZnO 1:1 (B). Four features are distinctly noteworthy. First, the dependences of τ_t and τ_r on light intensity follow a similar power law. Second, after the HAc treatment, the charge transport rate and recombination kinetics described by τ_t and τ_r, respectively, both become slower. Third, electron collection efficiency determined by the gap between τ_t and τ_r remains high (>90%) for film samples both before and after HAc treatments. Finally, τ_t and τ_r for the SnO$_2$/ZnO 1:1 composite film (Figure 11B) are obviously more affected by the HAc treatment than those for

High-Efficiency Dye-Sensitized Solar Cells

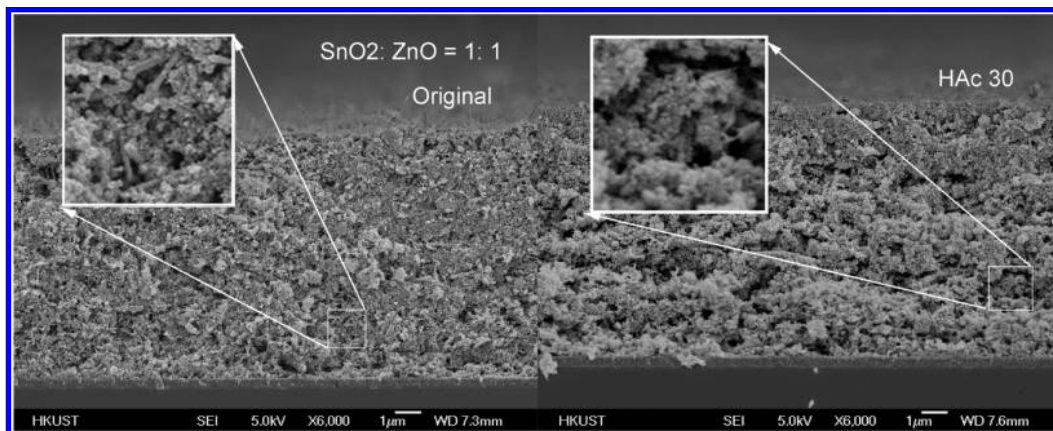*J. Phys. Chem. A, Vol. 114, No. 9, 2010* **3135**

Figure 9. Cross section view SEM images showing the structural differences between the original SnO₂/ZnO 1:1 composite film (original) and the corresponding HAc30 film. Note that corrosion of ZnO nanotetrapods leads to a more porous structure with less continuity in SnO₂ nanoparticles network.
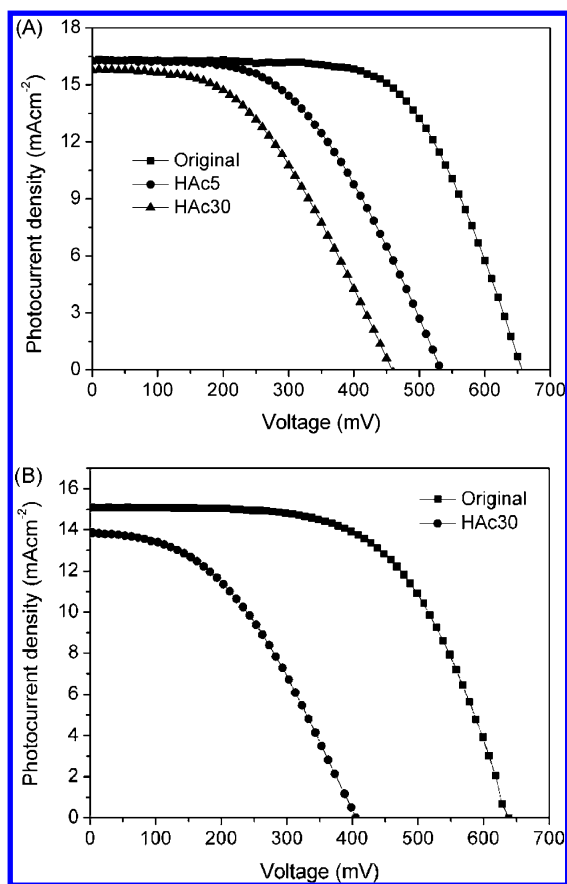

Figure 10. (A) $J-V$ characteristic curves of the original SnO₂/ZnO nanotetrapods 2:1 composite film and the corresponding HAc5 and HAc30 films. (B) $J-V$ characteristic curves of the original SnO₂/ZnO nanotetrapods 1:1 composite film and the corresponding HAc30 film.

the SnO₂/ZnO 2:1 composite film (Figure 11A). In the following, we give an in-depth discussion on these aspects in order.

3.4.1. Power Law Dependence of Transport and Recombination on Light Intensity. The power law dependence of τ_t on light intensity is well documented in dye-sensitized TiO₂ nanoparticle solar cells[10,12,14] and can be explained in terms of a multiple trapping model.[54] In brief, electrons enacting a random walk between trap sites have a power law distribution of waiting (detrapping) times in the form of $t^{-(1+\alpha)}$, leading to a power-law dependence of τ_t on light intensity: $\tau_t \propto I_0^{\alpha-1}$, where α describes the steepness of the trap-state distribution (0−1).[55,56]

Given that electrons in semiconductor need to migrate to the surface recombination centers in a similar trapping−detrapping fashion, a general proportional relationship between τ_r and τ_t is expected ($\tau_r \propto \tau_t$).[57] Our experimental observation agrees with such a relationship, although the slopes of the dependences of τ_t and τ_r on light intensity are slightly different (Figure 11), which has also been commonly previously reported.[58,59]

3.4.2. Decelerated Transport and Recombination due to HAc Treatment. In Figure 11, associated with the gradual attrition of ZnO nanotetrapods and ZnO shells is an obvious increase in the slopes (α-1). Because a larger α is correlated with a narrower trap distribution,[57] the HAc-treated films resemble the pure SnO₂ nanoparticles films in that they possess narrower trap distributions than their original films. The question as to whether the wider trap distributions in the original films can be attributed to ZnO nanotetrapods or ZnO shells is left for discussion below.

Particularly interesting is the decrease in recombination rate (inversely proportional to τ_r) for the HAc-treated films in comparison with their original films. Interestingly, such a decreased recombination rate is accompanied by the decreased V_{oc} for the HAc-treated films, as shown in Figure 9. This phenomenon is at variance with the suggestion that V_{oc} of SnO₂/ZnO composite photoanode is augmented in comparison with pure SnO₂ photoanode due to recombination suppression.[7,8] Instead, we believe, the real reason behind the V_{oc} enhancement lies in the ZnO-shell-induced negative shift of the conduction band edge of SnO₂, as proposed by Niinobe et al.[35] The negative shift of the conduction band edge for the composite films can be understood by the existence and direction of a Sn−O−Zn dipole at the core−shell interface, in which Sn⁴⁺ has a higher electrophilicity than Zn²⁺, and thus electrons tend to move from the ZnO shell to the SnO₂ core, ultimately raising the conduction band edge of SnO₂.[60] Indeed, this is supported by a binding energy downshift of the Sn 3d₅/₂ XPS peak, that is, an upshift of the energy level toward the vacuum level, with the increase in the ZnO shell thickness (Figure 3 and Figure S6 of the Supporting Information), in much the same way as observed by Niinobe et al.[35] In a previous work, ZnO shelled on TiO₂ nanoparticles yielding higher V_{oc} of the corresponding solar cell than bare TiO₂ has also been attributed to band edge movement rather than barrier layer effect on recombination.[60]

3.4.3. Generally High Charge Collection Efficiency. For the SnO₂/ZnO 2:1 composite film, the charge collection efficiency (estimated from τ_t and τ_r) is nearly unaffected by the HAc treatment, close to 100%. Plausibly, in the nearly pure SnO₂
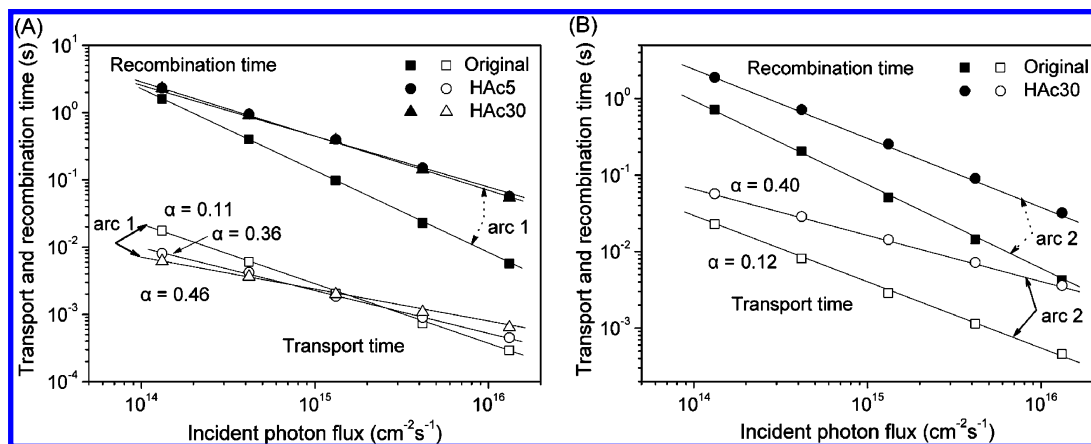
Figure 11. Incident light-intensity-dependent transport and recombination time constants. (A) Original SnO$_2$/ZnO nanotetrapods 2:1 composite film and the corresponding HAc5 and HAc30 films and (B) original SnO$_2$/ZnO nanotetrapods 1:1 composite film and the corresponding HAc30 film. Arcs 1 and 2 highlight the differences in electron transport time (solid arc) and recombination time (dotted arc) caused by HAc treatment for the two different composite photoanodes, respectively. The straight lines represent power-law fits. α values are calculated from the logarithmic slopes (α-1) by least-squares fitting.

nanoparticles film (HAc30 film), although the electron transport time is relatively long, the electron lifetime is similarly long, leading to the insensitivity of charge collection efficiency on the HAc treatment. This explains why J_{sc} for the SnO$_2$/ZnO 2:1 composite films with nearly the same dye-adsorbing amount (Figure S7, Supporting Information) has almost no change after HAc treatments (Figure 10A). Similarly, nearly no change occurs to the charge collection efficiency for the SnO$_2$/ZnO 1:1 composite film (~90% at the highest light intensity), presumably for the same reason discussed above. However, there is a pronounced decrease in J_{sc}, which for the HAc30 film is ~20% lower than that of the original SnO$_2$/ZnO 1:1 composite film (Figure 10B). Because charge collection remains a nearly constant efficiency as described above, the decrease in J_{sc} is mostly ascribable to the reduced dye-adsorbing amount, from (2.0 to 1.6) × 10^{-7} mol cm^{-2} according to our dye-desorption measurements, which is induced by the corrosion of a much higher ZnO nanotetrapods content than that in the SnO$_2$/ZnO 2:1 composite film. The reduction of J_{sc} from the original SnO$_2$/ZnO 1:1 composite film to its corresponding HAc30 film implies that the electrons from ZnO nanotetrapods contribute to the total J_{sc} of the composite film; namely, photoinjected electrons from the dye adsorbed on ZnO nanotetrapods can flow fluently to the SnO$_2$ nanoparticles network.

3.4.4. Effects of Film Composition. As mentioned above, for the SnO$_2$/ZnO 1:1 composite film, the increase in τ_t and τ_r due to HAc treatment is much more significant than those of the SnO$_2$/ZnO 2:1 composite film (see arcs 1 and 2 in Figure 11 for the different magnitudes). A larger change of τ_t (solid line arc 2 in Figure 11B) for the SnO$_2$/ZnO 1:1 composite film because of HAc treatment than that of the SnO$_2$/ZnO 2:1 film (solid line arc 1 in Figure 11A) is believed to arise from the removal of more ZnO nanotetrapods in the former sample, leading to a less continuous film with a smaller connectivity and therefore a more tortuous electron diffusion pathway in it. A higher porosity means that more nanoparticles are suspended with less neighboring nanoparticles in the SnO$_2$/ZnO 1:1 HAc30 film than those in the SnO$_2$/ZnO 2:1 HAc30 film. The reduced interparticles communication leaves an increased possibility for the recombination of photoinjected electrons. Therefore, the change in τ_r (dotted line arc 2 in Figure 11B) for the SnO$_2$/ZnO 1:1 HAc film is obviously larger than that for the SnO$_2$/ZnO 2:1 HAc film (dotted line arc 1 in Figure 11A). A similar argument about the effect of porosity (or number of neighboring

nanoparticles) of TiO$_2$ nanoparticles films on the electron transport and recombination kinetics has been previously put forward.[61] To come to the point, the changes in τ_t and τ_r caused by the dissolution of ZnO nanotetrapods prove that the ZnO nanotetrapods play an import role in the charge transport and recombination kinetics of our composite films.

3.5. More on the Electric Role of ZnO Nanotetrapods in the Composite Films. From the discussion above, it is still unclear as to what extent ZnO nanotetrapods separately impinge on electron transport and recombination kinetics irrespective of the ZnO shell thickness on SnO$_2$ nanoparticles because both the corrosion of ZnO nanotetrapods and the decrease in the ZnO shell thickness occur simultaneously during the HAc treatment. As a further question, what are the benefits associated with the structural advantages of ZnO nanotetrapods over ZnO particles used previously in SnO$_2$/ZnO composite films?[6,8] With these questions in mind, we opted to study two reference composite films (5.0 ± 0.2 µm thick) prepared by blending our SnO$_2$ nanoparticles separately with two types of ZnO particles, one with a size of ~40 nm (synthesized according to the literature[62]) and another with a size of about 500 nm (commercially available). The weight ratios of the two reference films were controlled at SnO$_2$/ZnO 2:1 for the sake of comparison with the SnO$_2$/ZnO nanotetrapods 2:1 composite film on transport and recombination kinetics. The large particles are similar to those that were employed in the literature,[6,8] whereas the small particles have a BET surface area of 25.6 m^2 g^{-1}, which is comparable to that of the ZnO nanotetrapods (BET = 18.9 m^2 g^{-1}), for which a similar dye-adsorbing amount can be expected. Advantageously, because the ultrathin ZnO shells on SnO$_2$ are similar in all of these films because of the similar preparation procedures used (this can also be appreciated from their similarly enhanced V_{oc}, all above 600 mV), the variation in transport kinetics can then be exclusively attributed to the changes of the ZnO particles or nanotetrapods in the composite films. To facilitate comparison, diffusion coefficient D_n as an intrinsic material property will be used in place of τ_t. It is calculated by $D_n \approx d^2/2.35\tau_t$,[25,63] where d is the film thickness. According to the relationship between D_n and τ_t, the dependence of D_n on light intensity (I_0) can also be described by a power law expression $D_n \propto (I_0)^{1-\alpha}$.[63]

D_n and τ_r dependences on the incident photon flux (light intensity, I_0) of the composite films are shown in Figure 12A,B side by side. Taken as a whole, Figure 12A highlights the
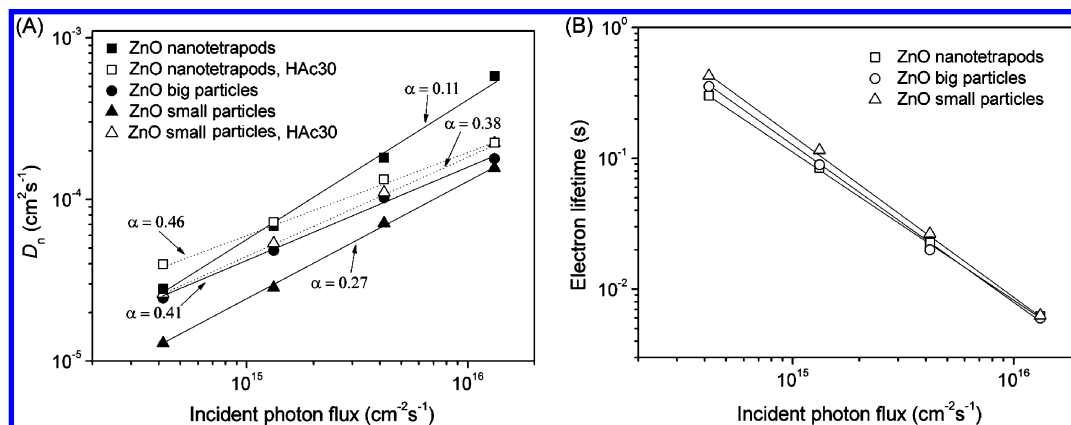
Figure 12. Incident light-intensity-dependent (A) electron diffusion coefficient D_n and (B) electron lifetime τ_r of the SnO_2/ZnO nanotetrapods 2:1 composite film and the two reference films with the ZnO nanotetrapods being replaced by ZnO small particles (40 nm) or ZnO big particles (500 nm). The straight lines represent power-law fits. α values are calculated from the logarithmic slopes (1-α) by least-squares fitting.

importance of morphologies of the ZnO additives in modulating the transport kinetics given the similar ZnO shelled SnO_2 nanoparticles for all of the composite films, whereas Figure 12B repudiates any substantial influence of such morphologies on the recombination kinetics, leaving behind the ultrathin ZnO shells on the SnO_2 nanoparticles as the main determinant of recombination kinetics in the composite films. In getting into more detail, we attend to a few important features in Figure 12A. First, D_n of the ZnO nanotetrapod-derived composite film is larger than those of the two reference films, especially that of the small ZnO particles reference film by a factor of 2.18 to 3.72 in the tested light intensity range. Second, the logarithmic slope (1−α) of D_n dependence on I_0 for the ZnO nanotetrapods derived composite film (α = 0.11) is much larger than those for the reference composite films (α = 0.27 for the small ZnO particles reference film; α = 0.41 for the big ZnO particles reference film, α = 0.41). Third, D_n for the small ZnO particles reference film is smaller than that of its corresponding HAc30 film, in marked contrast with the fact that D_n for the ZnO nanotetrapod-derived composite film is mostly larger than that of its corresponding HAc30 film.

The larger D_n value and the larger logarithmic slope of D_n dependence on light intensity for the ZnO nanotetrapod-derived composite film are clear advantages for charge collection over the two ZnO particles reference films, which become even more apparent under close-to-one sun light illumination (the highest light intensity employed in our IMPS/IMVS study was only ~1/20 sun). This is consistent with our experimental observation that under similar film fabrication and solar cell test conditions the cell performance for the ZnO-particle-derived composite films proved to be inferior to that for our ZnO nanotetrapods/ SnO_2 nanoparticles composite films.

The sharp contrast between the HAc-induced increase in D_n for the small ZnO particles reference film and the HAc-induced decrease in D_n for the ZnO nanotetrapod-derived composite film connotes a "relay transport" mechanism in the composite films. In a "relay transport" scenario, photoinjected electrons are free to move from SnO_2 nanoparticle regions to ZnO additive regions and vice versa and finally reach the conductive glass substrate, contributing to the overall J_{sc} of the solar cell. In fact, we have already demonstrated above the injection of electrons generated by the photoexcited dyes adsorbed on ZnO nanotetrapods into SnO_2 nanoparticles matrix and the attendant contribution to the overall J_{sc}. Now the question is whether the opposite electron injection, for example, from SnO_2 nanoparticles to ZnO nanotetrapods, is possible. We argue that if only the ZnO-to-SnO_2

electron injection was allowed but the reverse was forbidden, then D_n values of the composite films should not have shifted toward the opposite directions upon the HAc treatment just because of different morphologies of the ZnO additives. In addition, the feasible electron injection from SnO_2 to ZnO is consistent with the ZnO shell-induced up-shift of the conduction band edge of the SnO_2 nanoparticles. We suspect that the opposing effects of small ZnO particles and ZnO nanotetrapod-derived composite films on electron transport can be attributed to the more numerous grain boundaries between small ZnO particles and SnO_2 nanoparticles; their lattice mismatch could engender electron traps,[30] impeding fast electron transport in the composite network. This result, in turn, highlights the structural benefit of our ZnO nanotetrapods in facilitating electron transport in the composite films because of the reduction of heteroparticle grain boundaries.

The recombination kinetics are mostly decided by their similar ZnO shells on SnO_2 instead of the morphology of ZnO crystalline additives because the amount of dye taken up by ZnO crystalline additives is much smaller than that by SnO_2 nanoparticles for all three composite films. Furthermore, for recombination, photoinjected electrons only need to diffuse to the outer surfaces of nanoparticles (particles) or nanotetrapods and hence the effect of the grain boundaries mentioned above is much less consequential, as evidenced by the similar recombination kinetics in Figure 12B for the different ZnO/ SnO_2 composite films.

4. Conclusions

By capitalizing on the material advantages of both ZnO nanotetrapods and SnO_2 nanoparticles, we have achieved energy conversion efficiencies well >6% for DSSCs based on composite photoanodes encompassing the two nanomaterials. Whereas ultrafine SnO_2 nanoparticles promise a significant high roughness factor of composite films, ZnO nanotetrapods with special structural features afford fast electron transport for photoanodes. In this work, three SnO_2 nanoparticles/ZnO nanotetrapod (SnO_2/ ZnO 2:1, 1:1, and 1:2) composite films have been tested, among which the SnO_2/ZnO 2:1 composite film has attained the best efficiency of 6.31% mainly due to its highest saturated J_{sc} achieved at thinnest thickness. For composite films with higher ZnO nanotetrapods content, because of the requirement of higher film thicknesses, charge collection losses appear to be a main limiting factor that compromises the benefit from their favorable light scattering ability. We have shown that a ZnO source, be

it from particles or nanotetrapods, tends to form a generally similar ultrathin ZnO shell on SnO_2 nanoparticles. By comparison, for studies using the IMPS/IMVS technique, the functional roles of the ultrathin ZnO shell and the ZnO nanotetrapods in the SnO_2/ZnO composite film have been further elucidated for the first time: (1) The ultrathin ZnO shell mainly determines the recombination kinetics rather than the transport rate in the composite films and can elevate the conduction band edge position of SnO_2, which is responsible for the higher V_{oc} of DSSCs based on SnO_2/ZnO composite films; (2) ZnO nanotetrapods do contribute to electron transport in a "relay transport" manner, and because of the minimal-to-moderate heteroparticle grain boundaries, electron transport kinetics is facilitated in the ZnO nanotetrapod-derived composite film, accentuating the structural and thus transport supremacy of our branched nanostructure over particles additives in the SnO_2/ZnO composite photoanodes. More generally, the motif of branched structure and ultrathin shelled bicontinuous network holds a great potential in future developments of nanostructured solar cells.

Supporting Information Available: Optical images of dye-adsorbed thick composite films before and after ammonia treatment, XRD patterns of composite film samples, TEM-EDX characterization on composite film, time-resolved emission decays of dye-sensitized three composite films, and XRD, TEM, XPS, and UV−vis absorption characterizations on a standard composite film before and after HAc treatment. This material is available free of charge via the Internet at http://pubs.acs.org.

References and Notes

(1) Oregan, B.; Gratzel, M. *Nature* **1991**, *353*, 737.
(2) Bai, Y.; Cao, Y. M.; Zhang, J.; Wang, M.; Li, R. Z.; Wang, P.; Zakeeruddin, S. M.; Gratzel, M. *Nat. Mater.* **2008**, *7*, 626.
(3) Butler, D. *Nature* **2008**, *454*, 558.
(4) Gratzel, M. *Chem. Lett.* **2005**, *34*, 8.
(5) Chiba, Y.; Islam, A.; Watanabe, Y.; Komiya, R.; Koide, N.; Han, L. Y. *Jpn. J. Appl. Phys.* **2006**, *45*, L638.
(6) Tennakone, K.; Kumara, G. R. R. A.; Kottegoda, I. R. M.; Perera, V. P. S. *Chem. Commun.* **1999**, 15.
(7) Kumara, G. R. R. A.; Tennakone, K.; Kottegoda, I. R. M.; Bandaranayake, P. K. M.; Konno, A.; Okuya, M.; Kaneko, S.; Murakami, K. *Semicond. Sci. Technol.* **2003**, *18*, 312.
(8) Kay, A.; Gratzel, M. *Chem. Mater.* **2002**, *14*, 2930.
(9) Senevirathna, M. K. I.; Pitigala, P. K.; D, D. P.; Premalal, E. V. A.; Tennakone, K.; Kumara, G. R. A.; Konno, A. *Sol. Energy Mater. Sol. Cells* **2007**, *91*, 544.
(10) Tan, B.; Toman, E.; Li, Y. G.; Wu, Y. Y. *J. Am. Chem. Soc.* **2007**, *129*, 4162.
(11) Zhang, Q. F.; Chou, T. R.; Russo, B.; Jenekhe, S. A.; Cao, G. Z. *Angew. Chem., Int. Ed.* **2008**, *47*, 2402.
(12) Saito, M.; Fujihara, S. *Energy Environ. Sci.* **2008**, *1*, 280.
(13) Yoshida, T.; Zhang, J. B.; Komatsu, D.; Sawatani, S.; Minoura, H.; Pauporte, T.; Lincot, D.; Oekermann, T.; Schlettwein, D.; Tada, H.; Wohrle, D.; Funabiki, K.; Matsui, M.; Miura, H.; Yanagi, H. *Adv. Funct. Mater.* **2009**, *19*, 17.
(14) Kim, Y. J.; Lee, M. H.; Kim, H. J.; Lim, G.; Choi, Y. S.; Park, N.-G.; Kim, K.; Lee, W. I. *Adv. Mater.* **2009**, *21*, 3668.
(15) Kwak, E. S.; Lee, W.; Park, N. G.; Kim, J.; Lee, H. *Adv. Funct. Mater.* **2009**, *19*, 1093.
(16) Chen, D. H.; Huang, F. Z.; Cheng, Y. B.; Caruso, R. A. *Adv. Mater.* **2009**, *21*, 2206.
(17) Zukalova, M.; Zukal, A.; Kavan, L.; Nazeeruddin, M. K.; Liska, P.; Gratzel, M. *Nano Lett.* **2005**, *5*, 1789.
(18) Chen, W.; Sun, X. D.; Cai, Q.; Weng, D.; Li, H. D. *Electrochem. Commun.* **2007**, *9*, 382.
(19) Law, M.; Greene, L. E.; Johnson, J. C.; Saykally, R.; Yang, P. D. *Nat. Mater.* **2005**, *4*, 455.
(20) Law, M.; Greene, L. E.; Radenovic, A.; Kuykendall, T.; Liphardt, J.; Yang, P. D. *J. Phys. Chem. B* **2006**, *110*, 22652.

(21) Martinson, A. B. F.; McGarrah, J. E.; Parpia, M. O. K.; Hupp, J. T. *Phys. Chem. Chem. Phys.* **2006**, *8*, 4655.
(22) Galoppini, E.; Rochford, J.; Chen, H. H.; Saraf, G.; Lu, Y. C.; Hagfeldt, A.; Boschloo, G. *J. Phys. Chem. B* **2006**, *110*, 16159.
(23) Feng, X. J.; Shankar, K.; Varghese, O. K.; Paulose, M.; Latempa, T. J.; Grimes, C. A. *Nano Lett.* **2008**, *8*, 3781.
(24) Liu, B.; Aydil, E. S. *J. Am. Chem. Soc.* **2009**, *131*, 3985.
(25) Zhu, K.; Neale, N. R.; Miedaner, A.; Frank, A. J. *Nano Lett.* **2007**, *7*, 69.
(26) Zhu, K.; Vinzant, T. B.; Neale, N. R.; Frank, A. J. *Nano Lett.* **2007**, *7*, 3739.
(27) Tan, B.; Wu, Y. Y. *J. Phys. Chem. B* **2006**, *110*, 15932.
(28) Ku, C. H.; Wu, J. J. *Appl. Phys. Lett.* **2007**, *91*, 093117.
(29) Martinson, A. B. F.; Hamann, T. W.; Pellin, M. J.; Hupp, J. T. *Chem.—Eur. J.* **2008**, *14*, 4458.
(30) Thavasi, V.; Renugopalakrishnan, V.; Jose, R.; Ramakrishna, S. *Mater. Sci. Eng., R* **2009**, *63*, 1.
(31) Jiang, C. Y.; Sun, X. W.; Tan, K. W.; Lo, G. Q.; Kyaw, A. K. K.; Kwong, D. L. *Appl. Phys. Lett.* **2008**, *92*, 143101.
(32) Kang, S. H.; Kim, J. Y.; Kim, Y.; Kim, H. S.; Sung, Y. E. *J. Phys. Chem. C* **2007**, *111*, 9614.
(33) Chen, W.; Zhang, H. F.; Hsing, I. M.; Yang, S. H. *Electrochem. Commun.* **2009**, *11*, 1057.
(34) Nozik, A. J.; Memming, R. *J. Phys. Chem.* **1996**, *100*, 13061.
(35) Niinobe, D.; Makari, Y.; Kitamura, T.; Wada, Y.; Yanagida, S. *J. Phys. Chem. B* **2005**, *109*, 17892.
(36) Qiu, Y. F.; Yang, S. H. *Adv. Funct. Mater.* **2007**, *17*, 1345.
(37) Ba, J. H.; Polleux, J.; Antonietti, M.; Niederberger, M. *Adv. Mater.* **2005**, *17*, 2509.
(38) Hore, S.; Nitz, P.; Vetter, C.; Prahl, C.; Niggemann, M.; Kern, R. *Chem. Commun.* **2005**, 2011.
(39) Ferber, J.; Luther, J. *Sol. Energy. Mater. Sol. Cells* **1998**, *54*, 265.
(40) Tian, Z. P.; Tian, H. M.; Wang, X. Y.; Yuan, S. K.; Zhang, J. Y.; Zhang, X. B.; Yu, T.; Zou, Z. G. *Appl. Phys. Lett.* **2009**, *94*, 031905.
(41) Ito, S.; Murakami, T. N.; Comte, P.; Liska, P.; Gratzel, C.; Nazeeruddin, M. K.; Gratzel, M. *Thin Solid Films* **2008**, *516*, 4613.
(42) Jing, B. W.; Zhang, H.; Zhang, M. H.; Lu, Z. H.; Shen, T. *J. Mater. Chem.* **1998**, *8*, 2055.
(43) Wang, Z. S.; Kawauchi, H.; Kashima, T.; Arakawa, H. *Coord. Chem. Rev.* **2004**, *248*, 1381.
(44) Nazeeruddin, M. K.; Kay, A.; Rodicio, I.; Humphrybaker, R.; Muller, E.; Liska, P.; Vlachopoulos, N.; Gratzel, M. *J. Am. Chem. Soc.* **1993**, *115*, 6382.
(45) Cameron, P. J. P., L. M.; Hore, S. *J. Phys. Chem. B* **2005**, *109*, 930.
(46) Gregg, B. A. P., F.; Ferrere, S.; Fields, C. L. *J. Phys. Chem. B* **2001**, *105*, 1422.
(47) Peng, B. J. G.; Jäger, C.; Haarer, D.; Schmidt, H. W.; Thelakkat, M. *Coord. Chem. Rev.* **2004**, *248*, 1479.
(48) Fukai, Y.; Kondo, Y.; Mori, S.; Suzuki, E. *Electrochem. Commun.* **2007**, *9*, 1439.
(49) Koide, N.; Islam, A.; Chiba, Y.; Han, L. Y. *J. Photochem. Photobiol., A* **2006**, *182*, 296.
(50) Katoh, R.; Furube, A.; Yoshihara, T.; Hara, K.; Fujihashi, G.; Takano, S.; Murata, S.; Arakawa, H.; Tachiya, M. *J. Phys. Chem. B* **2004**, *108*, 4818.
(51) Koops, S. E.; Durrant, J. R. *Inorg. Chim. Acta* **2008**, *361*, 663.
(52) Koops, S. E.; O'Regan, B. C.; Barnes, P. R. F.; Durrant, J. R. *J. Am. Chem. Soc.* **2009**, *131*, 4808.
(53) Oekermann, T.; Zhang, D.; Yoshida, T.; Minoura, H. *J. Phys. Chem. B* **2004**, *108*, 2227.
(54) Frank, A. J.; Kopidakis, N.; van de Lagemaat, J. *Coord. Chem. Rev.* **2004**, *248*, 1165.
(55) Bisquert, J.; Vikhrenko, V. S. *J. Phys. Chem. B* **2004**, *108*, 2313.
(56) Nelson, J.; Chandler, R. E. *Coord. Chem. Rev.* **2004**, *248*, 1181.
(57) Kopidakis, N.; Benkstein, K. D.; van de Lagemaat, J.; Frank, A. J. *J. Phys. Chem. B* **2003**, *107*, 11307.
(58) Fisher, A. C.; Peter, L. M.; Ponomarev, E. A.; Walker, A. B.; Wijayantha, K. G. U. *J. Phys. Chem. B* **2000**, *104*, 949.
(59) Zhang, D. S.; Yoshida, T.; Oekermann, T.; Furuta, K.; Minoura, H. *Adv. Funct. Mater.* **2006**, *16*, 1228.
(60) Diamant, Y.; Chappel, S.; Chen, S. G.; Melamed, O.; Zaban, A. *Coord. Chem. Rev.* **2004**, *248*, 1271.
(61) Benkstein, K. D.; Kopidakis, N.; van de Lagemaat, J.; Frank, A. J. *J. Phys. Chem. B* **2003**, *107*, 7759.
(62) Demir, M. M.; Munoz-Espi, R.; Lieberwirth, I.; Wegner, G. *J. Mater. Chem.* **2006**, *16*, 2940.
(63) van de Lagemaat, J.; Frank, A. J. *J. Phys. Chem. B* **2001**, *105*, 11194.

JP908747Z